Vortex-Sheet Modeling of Hydrodynamic Instabilities Produced by an Oblique Shock Interacting with a Perturbed Interface in the HED Regime

S. Pellone,[1] C. A. Di Stefano,[2] A. M. Rasmus,[2] C. C. Kuranz,[1] and E. Johnsen[1]
[1)] *University of Michigan, Ann Arbor, MI 48109, USA*
[2)] *Los Alamos National Laboratory, Los Alamos, New Mexico 87544, USA*

(Dated: 6 December 2020)

We consider hydrodynamic instabilities produced by the interaction of an oblique shock with a perturbed material interface under high-energy-density (HED) conditions. During this interaction, a baroclinic torque is generated along the interface due to the misalignment between the density and pressure gradients, thus leading to perturbation growth. Our objective is to understand the competition between the impulsive acceleration due to the normal component of the shock, which drives the Richtmyer-Meshkov instability, and the shear flow across the interface due to the tangential component of the shock, which drives the Kelvin-Helmholtz instability, as well as its relation to perturbation growth. Since the vorticity resulting from the shock-interface interaction is confined to the interface, we describe the perturbation growth using a two-dimensional vortex-sheet model. We demonstrate the ability of the vortex-sheet model to reproduce roll-up dynamics for non-zero Atwood numbers by comparing to past laser-driven, HED experiments. We determine the dependence of the interface dynamics on the tilt angle, and propose a time scaling for the behavior at early time. Eventually, this scaling will serve as a platform for the design of future experiments. This study is the first attempt to incorporate into a vortex-sheet model the time-dependent interface decompression and the deceleration (and corresponding Rayleigh-Taylor instability) arising from laser turn-off.

I. INTRODUCTION

The growth of perturbations due to hydrodynamic instabilities at material interfaces plays an important role in the evolution of high-energy-density systems (HED), as it initiates multi-material mixing, possibly altering the overall flow dynamics of such systems. In inertial confinement fusion, for example, the growth of Rayleigh-Taylor[1,2] (RT), Richtmyer-Meshkov[3,4] (RM), and Kelvin-Helmholtz[5,6] (KH) instabilities may cause the outer cold ablator material to mix with the central hot spot, thus degrading the performance of capsule implosions.[7,8] At larger scales, the development of RT and RM instabilities in core-collapse supernovae also cause material mixing.[9,10] The KH instability plays a critical role in the development of turbulent boundary layers in planetary atmospheres.[11] Under HED conditions, shock-driven instabilities have been investigated at high-energy lasers by depositing kilojoules of laser energy into millimiter-size targets, leading to instabilities growing over nanoseconds.[12–15]

Beyond the early linear stage, the flow dynamics resulting from the growth of these instabilities sometimes involve combined effects of RM, RT, and/or KH.[16] Much of the past work on shock-driven perturbation growth at interfaces has emphasized a single one of these instabilities;[17–21] less attention has been paid to combinations. In the conventional RM instability, the shock front propagates in the direction normal to the mean interface, thereby causing an impulsive acceleration.[22–28] In a shock-driven KH geometry, the shock front propagates in the direction tangential to the mean interface, producing a shear across the interface.[29–35] The intermediate case of a mean interface tilted with respect to the incident shock wave, or an oblique shock interacting with an interface, introduces elements of shear in addition to the impulsive acceleration from the shock, such that both RM and KH contribute to perturbation growth.

Rasmus et al.[36,37] showed that varying the tilt angle alters the relative importance of KH and RM in their HED experiments. However, they studied only a small number of initial conditions and their model did not include post-shock baroclinic vorticity generation effects, which occur due to the misalignment of the density gradient across the interface with the pressure gradient across the incident shock. The late-time, non-linear dynamics of perturbation growth are characterized by the formation of large vortical structures, which dominate and eventually drive the mixing. Baroclinic vorticity generation alters the formation of these structures, and is therefore critical to include in the description of the non-linear perturbation growth. Of particular interest for this work is the post-shock generation of baroclinic vorticity due to the self-induced acceleration of the interface and vorticity transport along the interface. As the shock interacts with the interface, a sheet of vorticity is generated along the interface due to the misalignment of the density gradient (across the interface) and the pressure gradient (across the shock).[38,39] This baroclinic torque causes interfacial perturbations to grow, eventually giving rise to familiar bubble and spike structures. Furthermore, in HED experiments, laser turn off gives rise to a rarefaction that can affect perturbation growth. Experimental studies of these phenomena in the HED regime require specialized facilities and expertise, and generally do not yield large amounts of data. Numerical simulations of shock-driven interfacial instabilities necessitate significant resolution and modeling of complex physics (laser-matter interaction, radiation-hydrodynamics, turbulence). Although such approaches are comprehensive in the physics they

account for, it is difficult to isolate specific contributions to perturbation growth, e.g., the role of vorticity dynamics.

The initial growth of perturbations can be determined from the interface velocity induced by this baroclinic torque. The relationship between vorticity and velocity, i.e., the Biot-Savart law,[40,41] allows the problem to be reduced to evolving the interface from an initial distribution of vorticity along the interface. Vortex-sheet models are uniquely designed to represent vorticity-dominated interfacial dynamics. This paradigm is computationally attractive as it provides a one-dimensional parametrization of a two-dimensional interface, which allows for a detailed description of roll-up behavior lacking in current theoretical models of both linear[3,42–44] and nonlinear[45–48] phases of the growth. In classical fluid dynamics, Rosenhead[49] considered the evolution of a vortex sheet discretized as a set of point vortices for the KH instability. Numerical difficulties associated with roll-up formation, leading to curvature singularity, have been investigated for cases with[50–53] and without[54–57] a density jump across the interface. The inclusion of a density jump in the vortex-sheet formulation complicates both the physical model and the numerical treatment of the equations, as additional, non-linear terms must be incorporated in the equation governing the time evolution of the vortex sheet. Previous studies have successfully investigated RT[58–61] and RM[62,63] instabilities using the vortex-sheet model with these additional terms. A challenge with vortex-sheet modeling lies in prescribing initial conditions as current strategies have been developed for traditional fluid systems.[64] Under HED conditions, however, the dynamics of vortex sheets have yet to be used, with the exception of the kinematics study of Rasmus et al.[37]

In this work, we use a vortex-sheet model to investigate the growth of interfacial perturbations subject to an oblique shock under HED conditions. HED-relevant initial conditions are prescribed based on complementary hydrodynamic simulations. To better understand the relative importance between impulsive acceleration and shear, we investigate the dependence of the interface morphology on the initial tilt angle. Furthermore, this work is the first account of using a vortex-sheet model to predict secondary effects from experimental laser turnoff, such as time-dependent interface deceleration and decompression, as opposed to prior vortex-sheet modeling of constant-acceleration RT instability.[58–61] The manuscript is organized as follows. First, we describe the vortex-sheet paradigm and the governing equations, along with a strategy allowing the determination of the vortex-sheet strength distribution following the passage of the shock. Next, we investigate the dynamics for a given tilt angle and density jump, corresponding to the experiments performed by Rasmus et al.[36,37] The role of the tilt angle on the perturbation growth is then examined, before ending with concluding remarks.

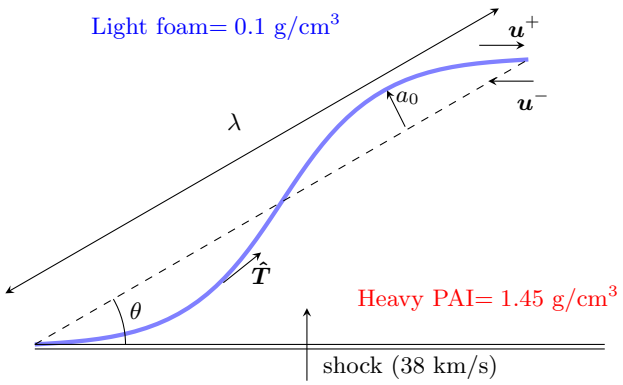

FIG. 1: Problem set-up for the interaction of an oblique shock with a perturbed interface.

II. GOVERNING EQUATIONS AND NUMERICAL DISCRETIZATION

During the interaction of a shock wave with a perturbed interface, a baroclinic torque is generated along the interface due to the misalignment between the density gradient across the interface, $\boldsymbol{\nabla}\rho$, and the pressure gradient across the shock wave, $\boldsymbol{\nabla}p$. The subsequent dynamics of the post-shock interface evolution can be described by the vorticity equation. The thin vortex sheet along the interface induces a velocity field given by the Biot-Savart law.[40,65] The subsequent evolution of this vortex sheet is obtained by following the trajectories of Lagrangian markers located on the sheet.[41] In this section, we describe the problem set-up, the physical/numerical models, and the initial conditions.

A. Problem set-up

The problem set-up, shown in Fig. 1, is based on the experiments of Rasmus et al.[36,37] performed on the OMEGA-EP laser facility on a target composed of a layer of polyamide-imide (PAI of density 1.45 g/cm^3) next to a layer of foam (density 0.1 g/cm^3), resulting in a pre-shock Atwood number $A_{\text{pre}} \approx 0.87$. A shock wave travels from the heavy material into the light material, and interacts with a two-dimensional sinusoidal perturbation (wavelength $\lambda = 100$ μm, initial amplitude $a_0 = 0.1\lambda$) tilted by an angle $\theta = 30°$ with respect to the shock. The shock speed is approximately 38×10^3 m/s and the post-shock Atwood number is $A \approx 0.67$. We take our baseline case to be $\theta = 30°$ and investigate the dynamics as the tilt angle is varied between $0° \leq \theta \leq 50°$.

B. Vortex-sheet model

We start by performing a Helmholtz decomposition of the velocity field into solenoidal (rotational) and dilata-

tional (irrotational) components. The equations governing the solenoidal component are solved using the vortex-sheet formulation described by Pozrikidis.[41] The high flow velocities in the experiments ($\sim 10^4$ m/s) result in high Reynolds numbers, such that viscosity can be neglected. Finally, the effect of gravity is too weak at these time and length scales to play a significant role in the evolution of the interface. A vortex sheet is defined as a singular distribution of vorticity across which the tangential component of the velocity is discontinuous, with a strength given by

$$\gamma = (\boldsymbol{u}^- - \boldsymbol{u}^+) \cdot \hat{\boldsymbol{T}}, \tag{1}$$

where $\boldsymbol{u}^+$ and $\boldsymbol{u}^-$ are the velocities in the light and heavy material, respectively, and $\hat{\boldsymbol{T}}$ is the unit tangential vector to the sheet. The equations governing the time evolution of the sheet are obtained by considering the self-induced velocity of the sheet $\boldsymbol{U}$, commonly chosen as the average of the fluid velocity on each side of the sheet, such that $\boldsymbol{U} = \frac{1}{2}(\boldsymbol{u}^+ + \boldsymbol{u}^-)$. In this case, the sheet velocity can be written in terms of the sheet strength as

$$\boldsymbol{U} = \frac{d\boldsymbol{x}}{dt} = \int_{\mathcal{C}} \boldsymbol{K}[\boldsymbol{x}(s,t) - \boldsymbol{x}(s',t)]\ \gamma(s',t) ds', \tag{2}$$

where $\boldsymbol{x}$ is a point on the sheet $\mathcal{C}$, s is the arclength parametrizing the sheet, and $\boldsymbol{K}$ is the two-dimensional desingularized kernel[55]

$$\boldsymbol{K} = \frac{1}{2\lambda} \begin{pmatrix} \dfrac{-\sinh[k(y-y')]}{\cosh[k(y-y')] - \cos[k(x-x')] + \delta^2} \\ \\ \dfrac{\sin[k(x-x')]}{\cosh[k(y-y')] - \cos[k(x-x')] + \delta^2} \end{pmatrix}, \tag{3}$$

where λ is the perturbation wavelength after the passage of the shock, k is the wavenumber, and δ is a numerical smoothing parameter introduced by Krasny.[55] When $\delta = 0$, the Cauchy principal value of the integral must be taken. In the present study, $\delta = 0.1$ is chosen.[59] If the sheet strength is independent of time, i.e., $d\gamma/dt = 0$, Eq. 2 can be solved with appropriate initial conditions and provides a purely kinematic description of the evolution of the sheet, as in Rasmus et al.[37] To take into account the dynamics, including non-zero Atwood number contributions, an additional equation governing the sheet strength γ is needed. This equation is obtained by taking the difference of the Euler equations across the sheet and projecting onto the tangential direction,[41,58] leading to

$$\frac{d\gamma}{dt} = -2A\left(\frac{d\boldsymbol{U}}{dt}\cdot\hat{\boldsymbol{T}} + \frac{1}{8}\frac{\partial\gamma^2}{\partial s} - \boldsymbol{g}(t)\cdot\hat{\boldsymbol{T}}\right) - \gamma\frac{\partial\boldsymbol{U}}{\partial s}\cdot\hat{\boldsymbol{T}}, \tag{4}$$

where $A = \frac{\rho^- - \rho^+}{\rho^+ + \rho^-}$ is the Atwood number. The three terms multiplying the Atwood number represent the change in vortex-sheet strength due to generation of baroclinic vorticity. The first term is the acceleration of a point on the interface $d\boldsymbol{U}/dt$ due to the self-induced motion of the sheet. The second non-linear term corresponds to the advection of the sheet strength with the jump velocity across the sheet measured in the tangential direction. These two terms can be combined together and represent the average of the fluid acceleration on each side of the sheet in the tangential direction.[52,58] The third term $\boldsymbol{g}(t)$ is a time-dependent acceleration accounting for the fact that the interface is not in an inertial reference frame. The fourth term represents the elongation of the sheet in the tangential direction. As explained in Sec. II C, the dilatational velocity component is modeled using a factor accounting for shock compression and decompression due to laser-turn off, the latter represented by the third term in Eq. 4.

Eqs. 2 and 4 constitute the vortex-sheet governing equations and are discretized by second-order finite differences, with the exception of the second term in Eq. 4, which is a non-linear flux term solved using the Godunov method.[53,60] The integral in Eq. 2 is discretized by using the midpoint rule. The coupled Eqs. 2 and 4 constitute a Fredholm equation of the second kind, whose solution is complicated by the presence of the term $d\boldsymbol{U}/dt$ on the right-hand-side of Eq. 4. This difficulty is resolved by following an iterative procedure.[58] The vortex sheet is initially discretized into N Lagrangian points with corresponding arclengths s_j, $j = 1, \ldots N$. The system of equations is advanced in time using an explicit second-order Runge-Kutta scheme. To provide sufficient spatial resolution to accurately describe the interface distortion and roll-up features at late time, a point insertion procedure is implemented based on the distance between neighboring points.[66] Although investigations of similar problems have been conducted in the past,[53,59] the present study is the first report of highly resolved computations for oblique interfaces under HED conditions.

C. Deceleration and decompression due to laser turn-off

In the context of the problem under consideration, compressibility has two primary effects. First, velocity changes are accompanied by pressure changes, which give rise to density changes. Second, local flow changes are communicated to the rest of the domain at a finite speed (e.g., waves interacting with target boundaries), by contrast to incompressible flow where this information propagation speed is effectively infinite. Volumetric changes in the compressible component due to shock compression and laser turn-off are modeled by a decompression factor prescribed from corresponding one-dimensional simulations; a corresponding acceleration term must also be added to the vortex-sheet equation. With regard to transient wave propagation effects, experimental data do not suggest that such effects take place over the relevant observation time. Experimental data further suggests that the shock recedes from the interface at a higher velocity than the interface velocity such that shock proximity

effects[67] can be neglected.

Upon laser turn-off, a rarefaction is launched into the system, interacting with the interface at $t \approx 5$ ns, leading to decompression and deceleration of the interface.[37] Both effects result in modifications of the perturbation growth. The decompression is accompanied by a gradient of velocity across the interface, thus stretching the interface in the streamwise direction, while the deceleration causes a pressure gradient opposite to the density gradient at the interface, such that the system is Rayleigh-Taylor unstable during the interaction with the rarefaction. This latter effect is represented by the third term on the right-hand-side of Eq. 4, and corresponds to a body force due to the non-inertial reference frame. The time-dependent acceleration profile $\boldsymbol{g}(t)$ is obtained from the interface velocity computed from one-dimensional simulations, using the radiation-hydrodynamics xRAGE code[68], as is shown in Fig. 2a. The time origin is taken to be when the shock reaches the interface, causing an impulsive interface velocity. Thereafter, the interface velocity increases slightly until $t \approx 5$ ns, after which it decreases, indicating the arrival of the rarefaction at the interface. Because of the heavy-to-light configuration, negative values of the acceleration give rise to the RT instability.

The effect of the interface decompression is taken into account by multiplying the perturbation amplitude by a decompression factor determined by the distance between two Lagrangian tracer particles relative to their distance during the RT-stable phase, i.e., before the arrival of the rarefaction. One tracer particle is located in the foam, while the other is located in the PAI material, each initially located 30 μm away from the interface. The position of each particle over time (y_{foam} and y_{PAI}) is obtained from 1D xRAGE simulations, such that the decompression factor is given by

$$\left| \frac{y_{\text{foam}}(t) - y_{\text{PAI}}(t)}{(y_{\text{foam}} - y_{\text{PAI}})_{\text{post-refract}}} \right|, \tag{5}$$

where the "post-refract" subscript denotes the state after all waves produced during the refraction have crossed the tracer locations, as shown in Fig. 2b. Before the incident shock reaches the tracer particle in the PAI material ($t < 0$), the decompression factor is constant, as none of the particles have moved. After the shock has passed over the PAI particle, the decompression factor decreases, due to the upward velocity of the PAI particle and the fact that the shock has not yet reached the particle in the foam. As the shock reaches the interface, a reflected rarefaction originates due to the heavy-to-light configuration, causing the particle in the PAI material to be accelerated towards the interface. During this time, there is also a transmitted shock propagating in the foam material, which reaches the tracer particle in the foam at $t \approx 0$ ns. As a result, this particle moves upward, increasing the decompression factor after $t = 0$ ns. After the reflected rarefaction has passed over the particle in the PAI material ($t \approx 1$ ns), the decompression factor remains constant, and corresponds to the RT-stable phase. After $t \approx 5$ ns, the decompression factor increases, indicating the arrival of the rarefaction from laser turn-off.

Using additional tracer particles initially located at ± 10 μm and ± 20 μm demonstrated that the decompression factor is not sensitive to the choice of initial tracer position (data not shown). The choice ± 30 μm is an example where the tracers are far enough from the interface that the mesh resolution at the interface is not an issue, but close enough to correctly represent the rarefaction conditions experienced by the interface structure.

Our approach has two important limitations. First, not only is the pressure field prescribed (via the decompression factor and the acceleration term), but it also comes from a purely 1D calculation. Second, transient wave-propagation effects (e.g., reflections from boundaries) are ignored. We therefore expect the present approach to be applicable for nominally 1D base flows in geometries such that wave-propagation effects can be neglected, which are reasonable assumptions in the problem of interest.

D. Initial vortex-sheet strength distribution

The initial conditions are determined by the shape of the interface and the corresponding distribution of the vortex-sheet strength along the interface immediately after the passage of the shock. Rasmus et al.[37] showed that in the experimental system the interface undergoes a marginal direct phase inversion, causing the interface to be compressed so strongly (by a factor of $\sim$20 of its original amplitude), that the post-shock shape of the interface can be considered flat.

We initialize the vortex-sheet strength distribution along the interface with the approach of Samtaney and Zabusky,[64] who showed that the circulation per unit length of the pre-shock interface is proportional, to first order, to the local angle between the incoming shock and the pre-shocked interface α as

$$\gamma \equiv \frac{d\Gamma}{ds} \approx \sigma \sin\alpha = \sigma \frac{dy}{ds}, \tag{6}$$

where σ is independent of the interface geometry but is a function of the material properties, the shock Mach number, and pressure ratios across the generated waves from the incident shock refraction at the interface. Note that the local angle α varies along the perturbed interface, whereas θ denotes the mean angle between the interface and the shock. The expression for σ provided by Samtaney and Zabusky[64] is not valid under HED conditions given the exceedingly strong shock and the non-ideal gas equation of state. Instead, to determine σ, we use xRAGE to extract the total circulation Γ, as done by Rasmus et al.,[37] where a diagnostic box surrounding the post-shock flat interface is used to compute the total circulation. Integrating Eq. 6 directly with respect to the

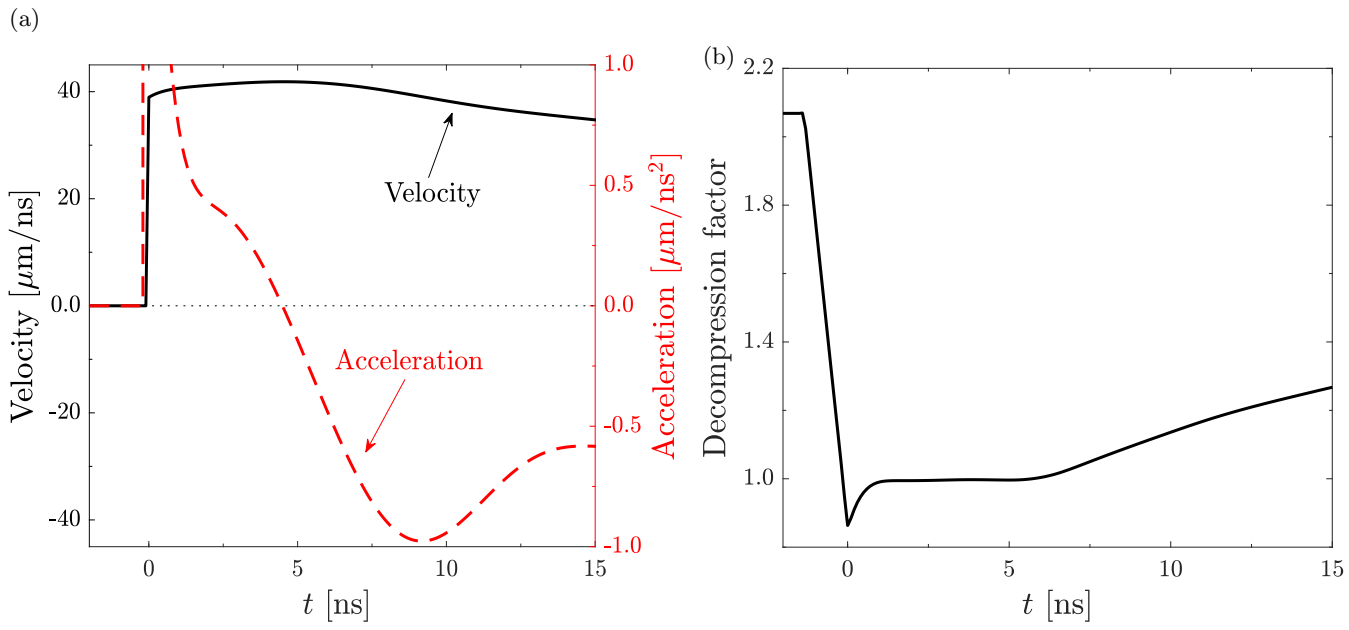

FIG. 2: Time evolution of (a) the interface velocity and corresponding acceleration, and (b) the interface decompression factor from xRAGE simulations.

unit length of the pre-shock interface ds would not yield the amount of circulation obtained from xRAGE, due to the compression of the interface. After an appropriate change of variable, it can be shown that $\Gamma = \int \gamma dx$. For $\theta = 30°$ and $\lambda = 100$ μm, we obtain $\Gamma = 1.4$ m^2/s and

$$\sigma = \frac{\Gamma}{\int \frac{dy}{ds} dx} = 4.3 \times 10^4 \text{ m/s}. \tag{7}$$

Fig. 3 shows the initial conditions for different tilt angles up to the critical value $\theta = 50°$ for initial amplitude $a_0 = 0.1\lambda$. Beyond this critical angle, part of the interface crosses the y-axis multiple times, in which case the assumption of a flat post-shock interface is not valid. In addition, higher-order terms need to be accounted for in Eq. 6 when the local angle α is too large. Such a scenario is beyond the scope of this study. Note that in the case $\theta = 30°$, the sheet-strength distribution is mainly negative, with only minor positive values at the extremities. A closer inspection reveals that the sheet-strength values are all negative for a tilt angle $\theta \gtrsim 32°$. In our study of the role of the tilt angle in section III B, the largest negative value of the initial sheet-strength distribution γ_0, seen in Fig. 3b, is used as a characteristic velocity to non-dimensionalize the time variable as $\tilde{t} = \gamma_0 t/\lambda$. For a given value of $\tilde{t} = 3$, the corresponding physical time is given in table I. We note that the perturbation in Fig. 3a is included for illustrative purposes; the present simulations are initialized with a flat interface and the sheet-strength distributions in Fig. 3b.

θ [°]	0	10	20	30	40	50
$\gamma_0 \times 10^4$ [m/s]	2.3	2.9	3.4	3.8	4.1	4.3
t [ns]	13	10	8.8	7.8	7.3	7.0

TABLE I: Maximum magnitude of vortex-sheet strength γ_0 and corresponding physical time for different tilt angles and $\tilde{t} = 3$.

III. RESULTS AND DISCUSSION

A. Dynamics of the baseline case

We first investigate the dynamics of our baseline case ($\theta = 30°$), including the role of interface deceleration and decompression due to laser turn-off. We also include, in Appendix A, a comparison to experiments and xRAGE simulations of the well-studied special case of $\theta = 0°$ (single-mode at normal incidence, i.e., RM instability[69]), which can be validated against existing well-established theory. The passage of the shock deposits vorticity along the interface, whose dynamics subsequently evolves according to the induced velocity field. Fig. 4 shows the post-shock time evolution of the interface and its associated sheet-strength distribution. The time evolution $t \leq 15$ ns corresponds to the experimental time range.[36,37] The width of each frame in Fig. 4a is $x/\lambda = 1$, but the post-shock interface wavelength corresponds to the effective wavelength $\lambda \cos\theta$, hence the extra space on the left and right of the interface.

As explained in the previous section and as supported by the experiments of Rasmus et al.,[37] the initial in-

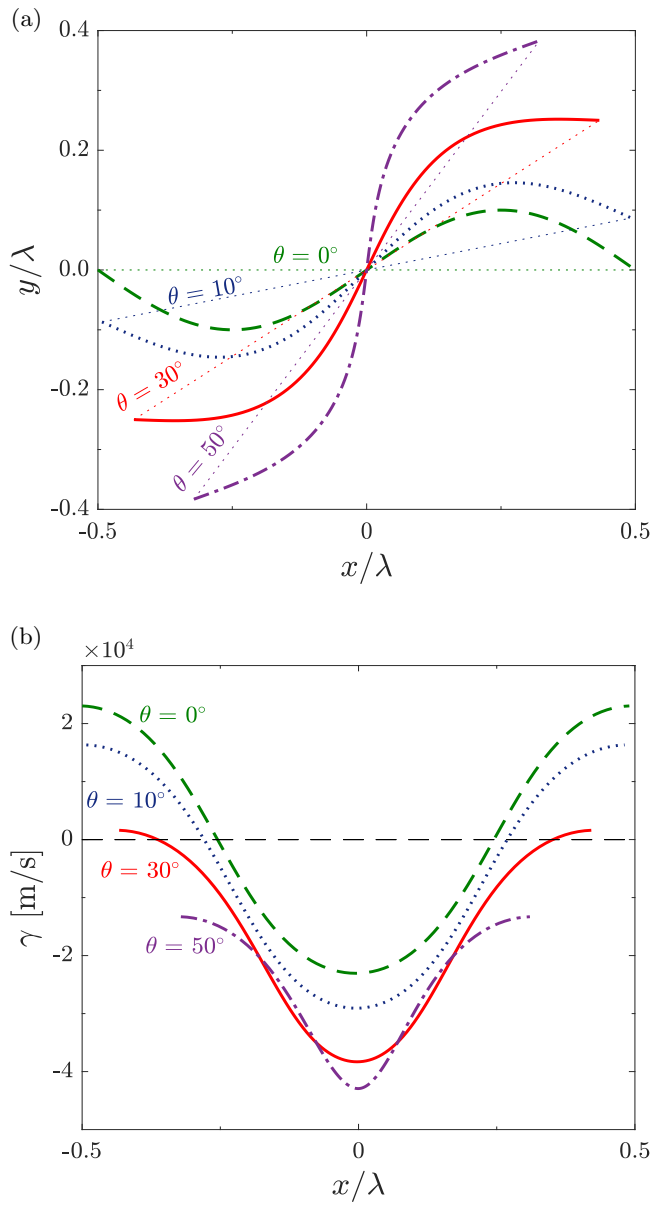

FIG. 3: (a) Pre-shock interface and (b) corresponding post-shock sheet-strength distribution for $0° \leq \theta \leq 50°$. The red line represents the baseline case ($\theta = 30°$).

terface morphology is initialized as flat, with a mean sheet-strength distribution that is negative. This negative mean sheet strength indicates mean clockwise rotation. The location of the largest negative value of the sheet strength achieved over the course of the simulation is denoted by s_-, and initially coincides with $s = 0.5 s_N$. This point separates the interface into two parts: the part between the arclength of the first point and s_- is referred to as the "left arm" of the interface, while the part between s_- and the last point is referred to as the "right arm" of the interface.

In the linear regime, the interface adopts a sinusoid-like shape (not shown for visualization purposes). The point s_- of the sheet-strength profile moves to the left and increases in magnitude, as the predominantly negative vorticity causes the left arm of the interface to rise and the right arm to sink. The point s_- is the point at which the average tangential component of the acceleration vanishes. The points on the left (right) of s_- have a positive (negative) average tangential acceleration, such that the points on each side of s_- move toward s_-, leading to an accumulation of vorticity near s_-. Heavy and light fluids start to penetrate each other.

By $t = 1.5$ ns, the perturbation amplitude is no longer small. The mean shear and mean negative vorticity cause the interface to start rolling up and become multivalued, i.e., for at least one x-coordinate along the interface there are two values of the corresponding y-coordinate. This first instance of a multivalued interface perturbation occurs along the right arm. Although gradually decreasing along the left arm, the rate of change of the sheet strength in s along the right arm changes abruptly at s_+ (inflection point), which eventually becomes the location of maximum positive strength.

After the interface has become multivalued, the perturbation rolls up, causing the interface to become multivalued along the left arm as well, and the crest to topple over, due to the large negative rotation at s_-. By $t = 5$ ns, the amount of heavy fluid separating the left and right arms on the rolled up side of the interface is vanishingly small, except for a blob near the vortex core. The roll-up has now a filament-like structure with the blob of primarily negative vorticity. At this time, the co-rotating vortex structure is evident. The centripetal acceleration causes the vorticity at s_+ to increase and eventually become positive.[70]

The large negative vorticity at and near s_- causes the blob to rotate with a local angular velocity, entraining some of the light fluid into the heavy fluid. As the blob rotates, its shape changes, and eventually breaks down into smaller blobs, which themselves rotate with their own angular velocity. More filament-like structures form, and by $t = 10$ ns, the angular momentum associated with the original blob causes un upward velocity of the now broken-down blob. As the latter keeps on breaking down, by $t = 12$ ns, the upward velocity causes this region of broken blobs to separate itself from the main mixing region. At these late times, three-dimensional and diffusive effects may alter the behavior of the interface by reducing the angular momentum of the rotating blob, which are beyond the scope of this study.

The interface morphologies shown in Fig. 4 can be used to produce synthetic radiographs. Approximating the densities of the heavy and light sides of the parametrized interface as the post-shock densities reported by Rasmus et al.[37], and modeling other properties of the radiograph, such as interface curvature,[69] yields the synthetic radiographs in Fig. 5. The time evolution corresponds to the experiments[37] (1 ns $\leq t \leq$ 11 ns) with increments of $\approx$ 1.32 ns. The result of this process is a blurring

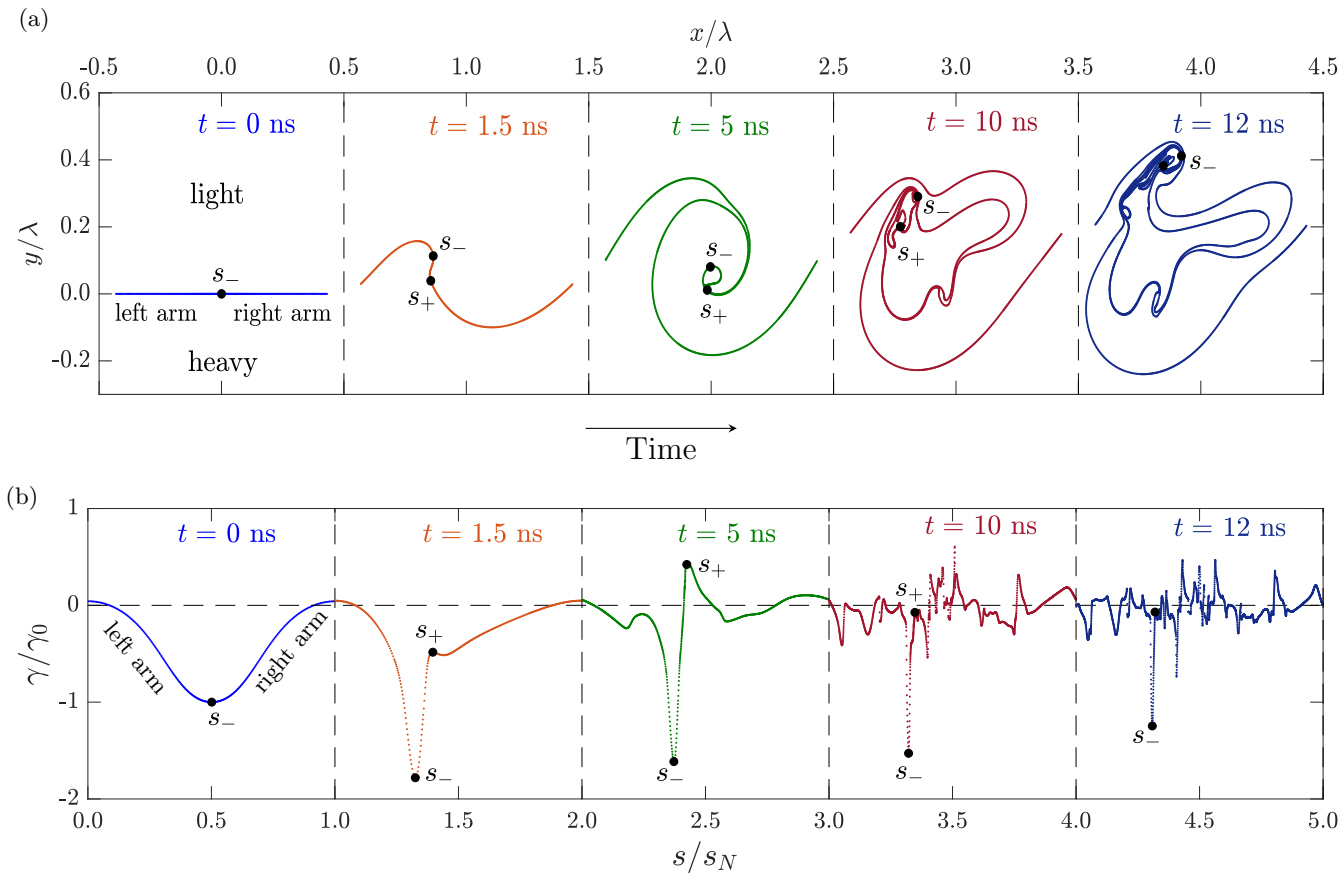

FIG. 4: Time evolution of (a) the interface morphology, and (b) its associated sheet-strength distribution along the interface arclength normalized by the total length of the interface (arclength value of the last point s_N) for the baseline case ($\theta = 30°$)

of the roll ups, thus making fine-scale filaments difficult to discern. In the experiments, the complicated structure of the roll-up at late times may seed smaller-scale 3D mixing, further blurring out the tips. This visualization demonstrates that blurry features observed in experimental radiographs could in fact be due to the finite resolution of the experimental diagnostics averaging out sub-pixel-scale flow dynamics, in addition to diffusion, as previously suggested.[71]

The above description of the time evolution of the vorticity distribution along the interface is important as it relates the interface morphology to the vorticity-dominated dynamics of the flow. Another important quantity is the time evolution of the mixing zone. Fig. 6 compares the time evolution of the perturbation amplitude obtained with the vortex-sheet model to the experiments of Rasmus et al.[37] Error bars of ± 3 μm accounting for the uncertainty in the measured amplitude, and ± 0.5 ns accounting for the uncertainty in the shock timing are added. To distinguish between the effects of volumetric changes and (incompressible) Rayleigh-Taylor-induced growth produced when turning off the laser, four cases are considered: the full dynamics, i.e., with deceleration and decompression due to laser turn-off, the dynamics ignoring deceleration, the dynamics ignoring the decompression, and the dynamics ignoring both the deceleration and decompression. Until the arrival of the rarefaction at 5 ns, the four solutions are close to each other; the solutions ignoring the acceleration term show slightly more rapid growth due to the increase of the interface acceleration in the absence of the positive acceleration present until $t \approx 5$ ns. Until this point, decompression and baroclinic vorticity due to the mean acceleration field do not play a prominent role in the perturbation growth; growth is primarily dictated by the baroclinic vorticity due to the self-induced vortex-sheet acceleration and its elongation. Once the rarefaction reaches the interface, discrepancies between the different solutions become manifest. Both RT acceleration and decompression contribute to growth during this interaction, as evidenced by the fact that the solution ignoring these two effects shows the largest discrepancy with the experiments. Accounting for RT acceleration (but ignoring decompression) only affects the growth at late times (after ~ 11 ns). For this problem, decompression plays a more prominent role in altering the perturbation amplitude growth start-

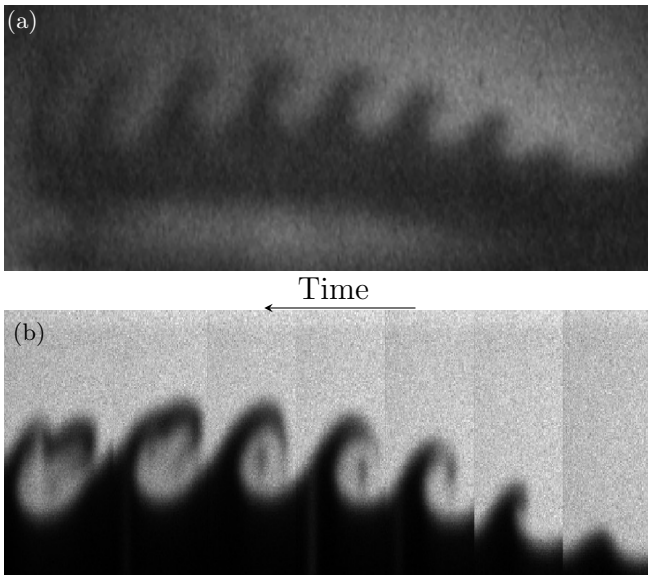

FIG. 5: Roll-up morphology of the baseline case ($\theta = 30°$) from (a) the experiments[37] (Reproduced from Rasmus, A. M. et al. "Shock-driven hydrodynamic instability of a sinusoidally perturbed, high-Atwood number, oblique interface." Physics of Plasmas 26.6 (2019): 062103, with the permission of AIP Publishing), and (b) reproduced synthetic image from vortex-sheet data.

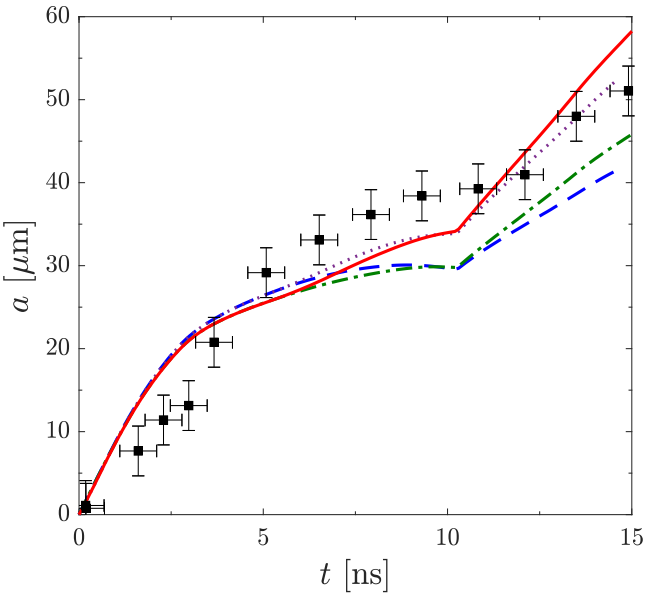

FIG. 6: Time evolution of the perturbation amplitude obtained from the vortex sheet, without laser-induced deceleration or decompression due to laser turn-off (- - -), with deceleration but without decompression (-·-·-), without deceleration but with decompression (·····), with both deceleration and decompression (——), and experiments[37](■).

ing at $t \approx 7$ ns. The late-time evolution of the perturbation growth is also altered by the above-mentioned upward velocity of the broken-down blob, resulting in a kink at $t \approx 10$ ns. This amplification of the growth is neither related to the RT acceleration nor to the decompression, since the solution ignoring these two effects exhibits the same behavior as well. Because of this growth amplification, the combination of RT acceleration and decompression produces a solution that slightly overpredicts the experimental results. The solution accounting for decompression (but ignoring RT acceleration) produces a solution closest to the experimental results. Discrepancies between the modeling and experimental results may be due to three-dimensional effects, the modeling of the decompression, equation-of-state effects, or diffusion effects.

B. Dependence of the dynamics on the tilt angle

Having related the interfacial dynamics to the vortex-sheet strength in the previous section, we now investigate the dependence of the interfacial dynamics on the tilt angle to understand the relative importance of impulsive acceleration vs. shear in the interface evolution. For simplicity, we neglect the effects of RT acceleration and interface decompression due to laser turn off. Upon inspection, the RT acceleration only has a minor effect on the roll-up morphology, and the interface decompression only scales the perturbation amplitude by the decompression factor.

1. Interface morphologies and vortex-sheet strength

As the tilt angle is increased, the pressure and density gradients become more misaligned, thus leading to an increased magnitude of the initial baroclinic torque. As confirmed by Fig. 3b, a larger tilt angle gives rise to a more skewed and narrow strength profile in the initial conditions. To perform a meaningful comparison when varying the tilt angle, we thus normalize time with the initial magnitude of the sheet strength γ_0, i.e., $\tilde{t} = \gamma_0 t/\lambda$. Figs. 7 and 8 show the time evolution of the interface morphology and its associated sheet strength until $\tilde{t} = 3$ for tilt angles between $0° \leq \theta \leq 50°$.

The case $\theta = 0°$ corresponds to the classical RM problem, which is characterized by the formation of counter-rotating vortices. The associated sheet-strength profile is initially symmetric with respect to the point s_0, which corresponds to the spike tip and point of zero vorticity; the interface remains symmetric about the vertical axis passing through this point and the sheet strength symmetric about this point. Tracking this point over time, the sheet strength is positive on the left of s_0, causing the interface to roll-up counterclockwise. On the right, the sheet strength is negative for the most part, eventually leading to clockwise roll up. This symmetry is sustained

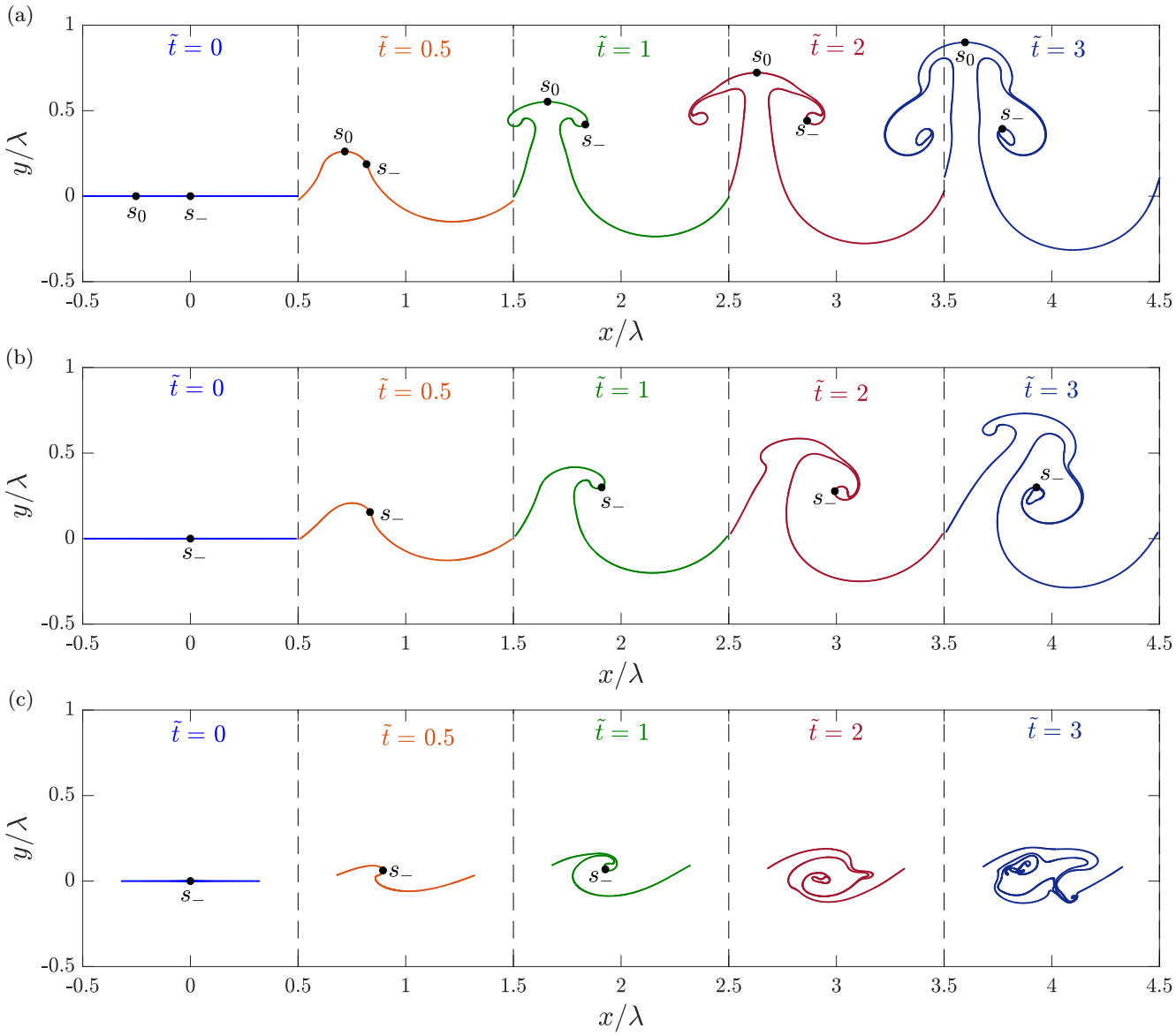

FIG. 7: Time evolution of the interface morphology for different tilt angles: (a) $\theta = 0°$ (RM), (b) $\theta = 10°$, (c) $\theta = 50°$. The left and right extremeties of the interface correspond to the effective wavelength $\lambda \cos\theta$.

over time and leads to two peaks of equal and opposite strength, which correspond to the core of each counter-rotating vortices.

For $\theta = 10°$, the interface first forms a clockwise roll-up until $\tilde{t} \approx 1$ due to the non-zero (negative) mean sheet strength. The positive contributions to the initial baroclinic vorticity along the interface are thus smaller than the negative contributions, such that the interface rolls up in the clockwise direction. A consequence is that there is no longer a symmetry point like s_o. Eventually ($\tilde{t} \approx 2$) the sheet-strength on the left arm forms a positive peak, corresponding to a counterclockwise roll-up. This peak and physical size of the roll up are smaller in magnitude than those corresponding to the clockwise roll-up on the right arm. At the largest tilt angle under consideration ($\theta = 50°$), the initial sheet strength has a mean that is more negative than for lower tilt angles. Only co-rotating vortices develop and eventually form an intricate pattern as the vortices roll over.

Fig. 9 shows the time evolution of the mean value of the sheet-strength profile for the tilt angles under consideration. The mean value of the sheet strength physically corresponds to the bulk shear flow across the interface. Initially, the mean sheet-strength increases in magnitude with the tilt angle due to the initial increased shear with the latter. For $\theta = 0°$, which corresponds to pure RM, the mean sheet strength is zero throughout and there is no bulk shear across the interface. For $\theta > 0°$, as

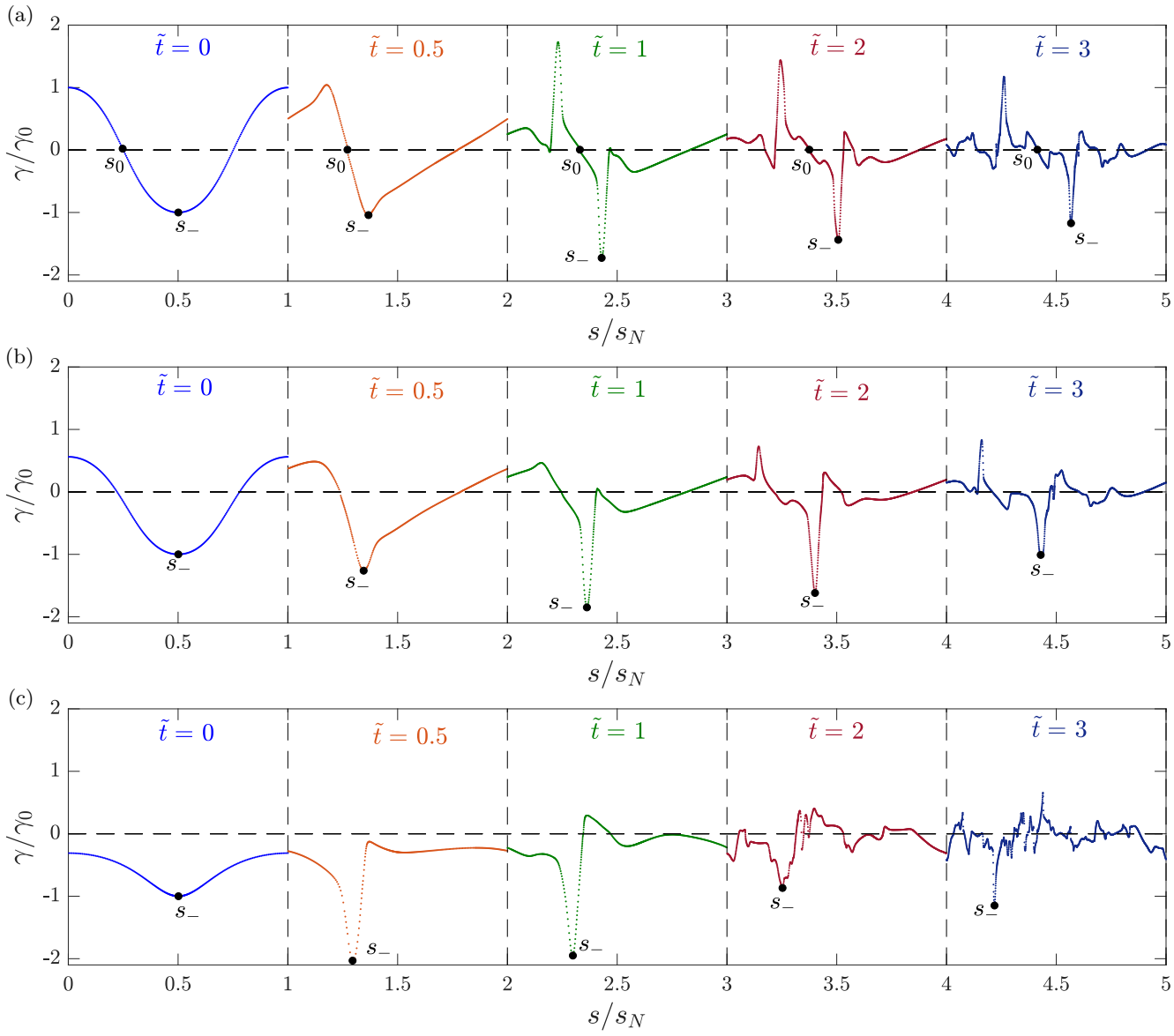

FIG. 8: Time evolution of the sheet-strength over the interface arclength for different tilt angles: (a) $\theta = 0°$ (RM), (b) $\theta = 10°$, (c) $\theta = 50°$. The arclength is normalized by the total length of the interface (arclength value of the last point s_N).

time progresses, the mean sheet strength becomes weaker and eventually reaches a non-zero asymptotic value, corresponding to a constant bulk shear flow. This reduction in magnitude of the sheet strength indicates that the amount of bulk shear decreases relative to its original value; the rate of decrease in strength magnitude is higher for higher tilt angles as the magnitude of the shear (characterized by a non-zero mean) is increased relative to that of the impulsive acceleration (characterized by the difference between the minimum and maximum of the initial distribution). The asymptotic value of the mean sheet strength increases with the tilt angle, except for $\theta = 30°$, which has a slightly larger value than that of $\theta = 50°$.

To better understand the role of shear vs. impulsive acceleration, Fig 10 shows the extrema of the sheet-strength profile with respect to its mean value for $0° \leq \theta \leq 50°$. Physically, the minimum sheet strength corresponds to the point of maximum vorticity in the flow (in magnitude) located at the vortex core, and is associated with the formation of the primary clockwise roll-up. Initially, the negative sheet strength amplitude relative to the mean increases (i.e., becomes more negative). This behavior is consistent with the observations of Rasmus et al.,[37] who showed that the mean value of the initial vorticity profile becomes larger than the variations in the

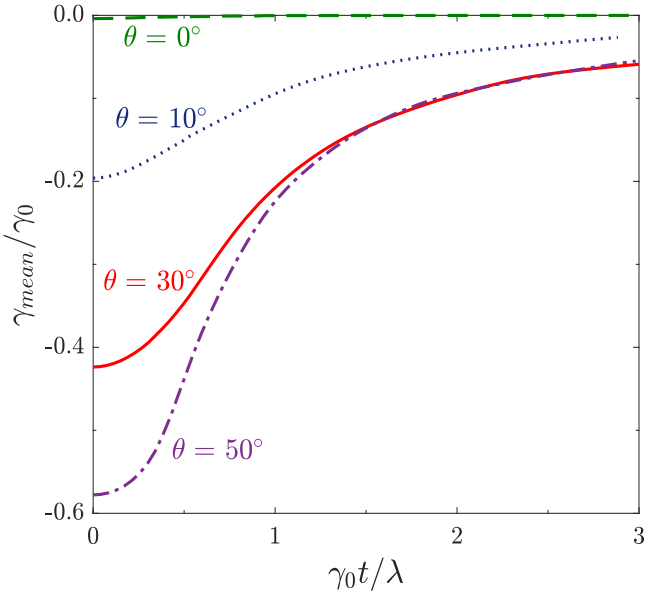

FIG. 9: Time evolution of the mean sheet-strength value for different tilt angles.

limit $\theta \to 90°$ (corresponding to pure KH). Eventually, each case reach a minimum in negative sheet strength, before decreasing in magnitude over time. This decrease is due to the development of opposite-sign vorticity associated with the centripetal acceleration of the roll-up, which cancels part of the primary vorticity. The maximum sheet-strength physically represents the point at which either a counterclockwise roll-up forms on the left arm, or opposite-sign vorticity develops. For $\theta = 0°$ and $10°$, the maximum sheet strength corresponds to the former and is located on the left of s_o, while for $\theta = 30°$ and $50°$, it corresponds to the latter and is located to the right of s_o. Note that for $\theta = 0°$, the evolution of the maximum and minimum relative strengths are the same due to the symmetry of the vorticity profile. Other than in the RM case, the largest negative strengths reach greater magnitudes than the maximum positive strengths. This preferential negative vorticity is a manifestation of the clockwise rotation imparted by the shear.

2. Early time scaling of the perturbation amplitude

When scaling time with the initial sheet strength, smaller perturbation growth is achieved over time with increasing tilt angle, as illustrated by Fig. 7. This behavior is quantitatively illustrated in Fig. 11, which shows the time evolution of the perturbation amplitude for $0° \leq \theta \leq 50°$. Here we investigate the early time growth of the perturbation and connect this behavior to the late time dynamics. Based on linear stability analysis of an oblique shock impinging upon a perturbed interface, Mikaelian[72] found that the perturbation amplitude behaves as

$$\frac{a(t)}{a_0} = \cosh(\omega t) + 2\frac{\Delta V}{\Delta U}\frac{A}{\sqrt{1-A^2}}\sinh(\omega t), \tag{8}$$

where a_0 is the initial perturbation amplitude, ΔV is the change in the velocity normal to the interface from the shock, ΔU is the difference in shear velocity across the interface, and ω is the KH growth rate

$$\omega = \frac{k\Delta U}{2}\sqrt{1-A^2}. \tag{9}$$

In the linear regime, ωt is small enough that Eq. 8 may be linearized as

$$\frac{a(t)}{a_0} = 1 + kA\Delta V t, \tag{10}$$

thus indicating that the perturbation amplitude does not depend on the shear velocity ΔU at early times. In this case, the decrease of the amplitude with the tilt angle may be explained from the initial profile of the vorticity distribution along the interface. In the case $\theta = 0°$, the initial vorticity profile is symmetric with respect to s_0 (see first frame of Fig. 8a). When evaluated from the y-component of Eq. 2, the contributions of the vorticity profile to the integral, from the first point to s_-, double the velocity at the tip of the spike s_0. Additionally, the contributions from s_- to the last point cancel out. In the oblique case, however, the negative mean value of the vorticity profile leads to a lower tip velocity magnitude.

Eq. 10 suggests a scaling of the perturbation amplitude in time by $k\Delta V$. In practice, ΔV is obtained using the post-shock velocity of the interface, u^*. Both ΔU and ΔV can be written in terms of the corresponding projection along the tangential and normal directions to the interface: $\Delta U = u^* \sin\theta$ and $\Delta V = u^* \cos\theta$. If $\theta = 0°$ and if there is no interfacial perturbation, the velocity u^* is given by the solution to the one-dimensional Riemann problem. Therefore, Eq. 10 can be written as

$$\frac{a(t)}{a_0} = 1 + kA(u^* \cos\theta)t. \tag{11}$$

For our purposes, since the sheet-strength magnitude γ_0 is the characteristic velocity, it is convenient to replace u^* by γ_0. Recalling Eq. 6, the rotation matrix from the tilted frame of reference (τ, η) to the (x, y) coordinate system allows the sheet strength to be written as

$$\gamma = \sigma\frac{dy}{d\tau}\frac{d\tau}{ds} = \sigma(\sin\theta + ka\cos\theta\cos(k\tau))\frac{d\tau}{ds}. \tag{12}$$

The maximum magnitude of the sheet-strength γ_0 is located at $\tau = 0$. Upon inspection, the term $d\tau/ds$ at $\tau = 0$ is close to unity for all tilt angles under consideration, with $(d\tau/ds)_{\tau=0} \approx 0.8$. Therefore, γ_0 can be written as

$$\gamma_0 \propto \sin\theta + ka\cos\theta. \tag{13}$$

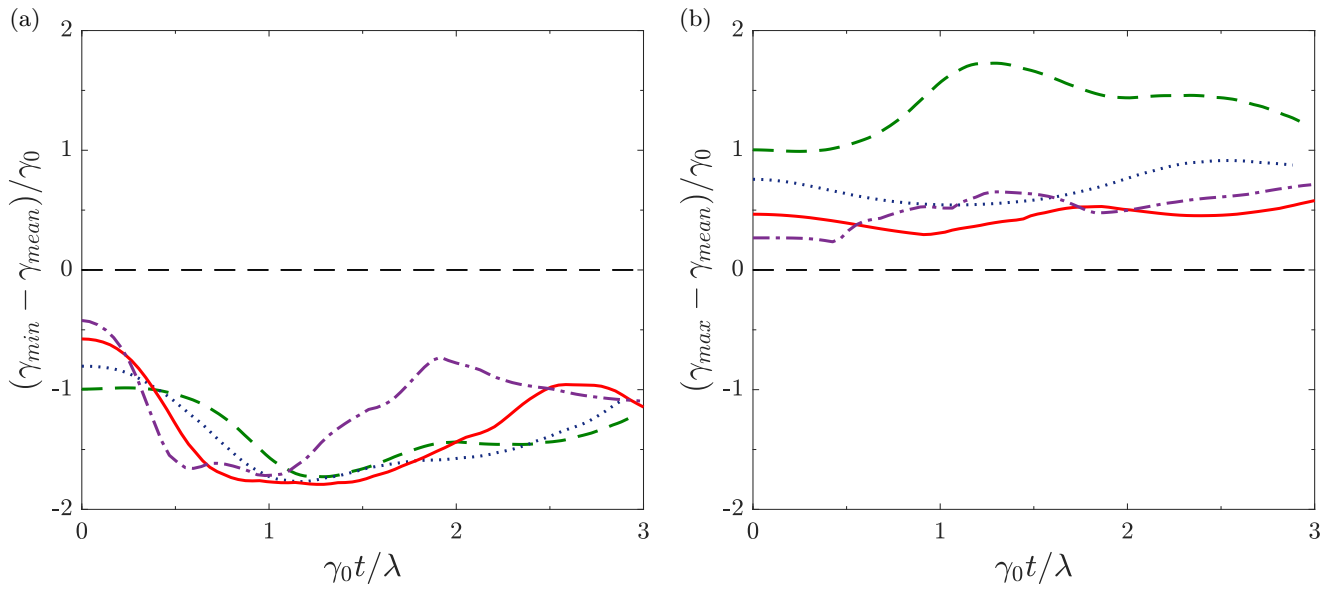

FIG. 10: Time evolution of (a) the minimum and (b) the maximum sheet-strength with respect to its mean value for $\theta = 0°$ (- - -), $\theta = 10°$ (·····), $\theta = 30°$ (——), and $\theta = 50°$ (-·-·-).

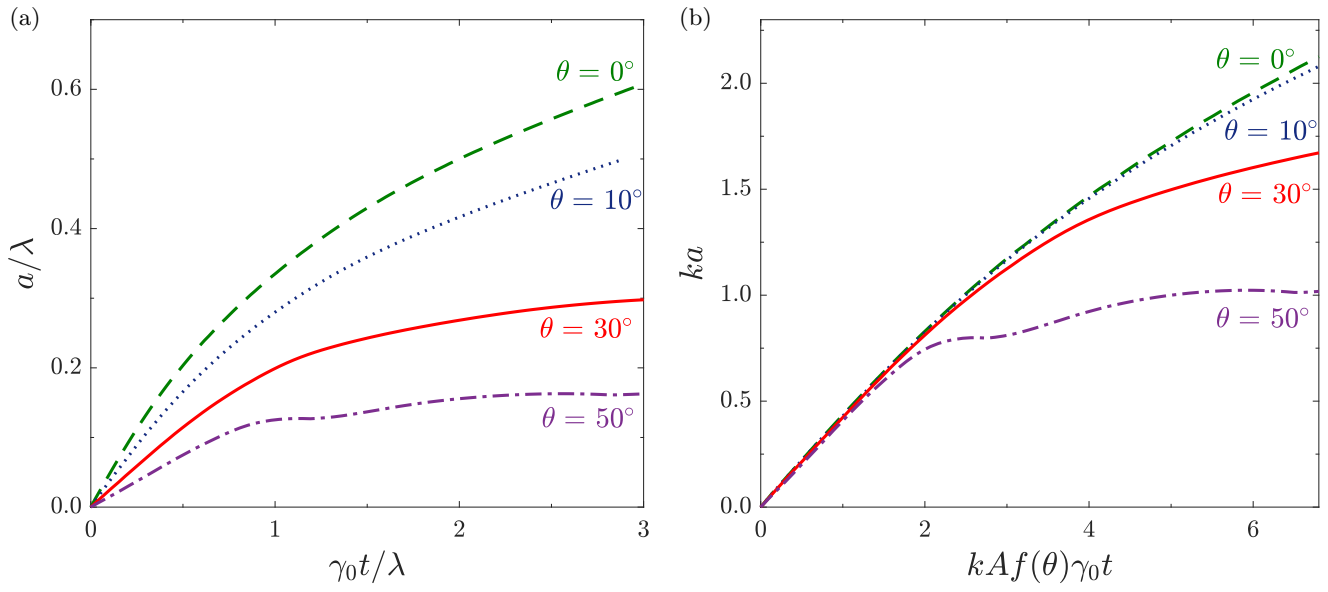

FIG. 11: Time evolution of the perturbation amplitude for different tilt angles when (a) unscaled, and (b) scaled using Eq. 14.

As such, we propose the following scaling in time of the perturbation amplitude with the tilt angle

$$\frac{a(t)}{a_0} = 1 + kAf(\theta)\gamma_0 t, \tag{14}$$

where $f(\theta) = \cos\theta/(\sin\theta + ka\cos\theta)$. Fig. 11b shows the growth for the different tilt angles, with time scaled by $kAf(\theta)\gamma_0$. The curves collapse at early times, thus illustrating the dominance of the impulsive acceleration (and its geometrical decomposition into normal and tangential components) early on. Eventually, shear becomes important, such that a greater tilt (and hence stronger shear), leads to an earlier departure from this behavior. Our analysis confirms and extends the conclusion drawn by Rasmus et al.[37] for the 30° case, namely that, for the HED problem under consideration, the instability is dominated at early times by RM, and at late times by shear. The effect of introducing a stronger shear is that

the overall amplitude at late times is smaller, because part of the momentum drives the instability in the transverse direction, leading to a reduced growth, compared to pure RM driven by a momentum in the streamwise direction. As observed in Fig. 7, the structure becomes complex more rapidly, which could have ramifications for transition to turbulence.

C. Kinematics vs. dynamics

The roll-up behavior is affected by the flow dynamics, which are coupled to the kinematics (Eq. 2) through Eq. 4. Past studies of this problem[37] assumed a constant sheet strength in time, thus effectively neglecting the dynamics. That study predicted that the roll-up develops symmetrically over time. As described in Sec. II B, the vortex-sheet dynamics are governed by two main mechanisms: baroclinic vorticity and sheet elongation. The former is pre-multiplied by the Atwood number: assuming $A = 0$ effectively neglects generation of baroclinic vorticity, such that the sheet evolves according to its elongation only (fourth term on the right-hand-side of Eq. 4). As such, we expect that the asymmetry of the roll-up originates from non-zero Atwood number effects. To demonstrate this behavior, we consider the interface evolution and the corresponding sheet strength for the baseline case with $A = 0$ (Fig. 12) and kinematics only (Fig. 13), in comparison to the full model with finite Atwood number (Fig. 4). In the baseline case with $A = 0$, the interface rolls up symmetrically with respect to its vortex core and the sheet-strength profile stays symmetric with respect to the mid-arclength over time. The only source of sheet-strength evolution is due to sheet-elongation, leading to an amplification of the sheet-strength magnitude at the vortex-core. Based on this observation, we conclude that the asymmetry in the roll-ups originates from finite Atwood number effects, namely the acceleration terms, which generate vorticity. When considering the kinematics only, the interface also rolls up symmetrically with respect to its vortex core and the sheet-strength profile is symmetric. However, the sheet strength being independent of time, there is no sheet-strength magnitude amplification due to sheet-elongation. As a result, the interface does not roll up as much as in the $A = 0$ case. This approach prohibits vorticity generation of any kind. Note that the sheet strength at the Lagrangian points and the total circulation do not change over time; the apparent changes in the shape of the strength in Fig. 13b are due to the increasing arc length in the region of high vorticity.

IV. CONCLUSIONS

In this work, we use a vortex-sheet model to investigate the interaction of an oblique shock with a perturbed interface in two dimensions under HED conditions. At early times, the pertubation growth is dominated by the impulsive acceleration of the shock (RM), as evidenced by our proposed scaling accounting for the normal and tangential components of the shock. At later times, the perturbation growth is modulated by the positive and negative vorticity generated by the shear and the decompression due to the arrival of the rarefaction produced by laser turn off. As the tilt angle is increased, the onset of the shear-dominated dynamics occurs earlier and becomes more pronounced. We further demonstrate how Atwood number effects break the symmetry in the flow. By appropriately prescribing the initial conditions, accounting for the body force corresponding to the accelerating reference frame, and incorporating the effect of decompression, reasonable agreement with experimental data is achieved.

Having shown the applicability of our vortex-sheet model to an instance of single-mode oblique instability, a possibility for further study is to investigate the role of the Atwood number on the perturbation growth. Another possibility is to investigate more-complex interface structure, such as multimode initial perturbations, relevant in practice, and their vorticity dynamics. The key challenge is to prescribe an accurate initial vortex-sheet strength distribution, which can be achieved using the model of Samtaney & Zabusky,[64] as well as an appropriate initial morphology. This approach is applicable to sufficiently small-amplitude perturbations for which the superposition principle can be leveraged. However, for finite-size perturbations, other strategies must be devised.

ACKNOWLEDGMENTS

This work was supported in part by the National Science Foundation under grant no. PHY-1707260 and by the Los Alamos National Laboratory under contract 89233218CNA000001 with Triad National Security LLC. The authors would like to acknowledge Prof. Krasny and Ling Xu for their valuable insights on the numerical implementation of the vortex-sheet model.

Appendix A: Single-mode Richtmyer-Meshkov instability

We compare our vortex-sheet model against the RM experiments of Di Stefano et al.,[69] along with the corresponding two-dimensional xRAGE simulations with a laser model.[73,74] The experimental conditions of Di Stefano et al.[69] are the same as those considered in the current work, with the exception that the initial tilt angle is $\theta = 0°$. Since the laser-turn-off conditions are the same, early RM growth is followed by RT growth once the rarefaction reaches the interface.

Fig. 14 compares the time evolution of the perturbation amplitude obtained with the vortex-sheet model (with and without laser-induced deceleration and decom-

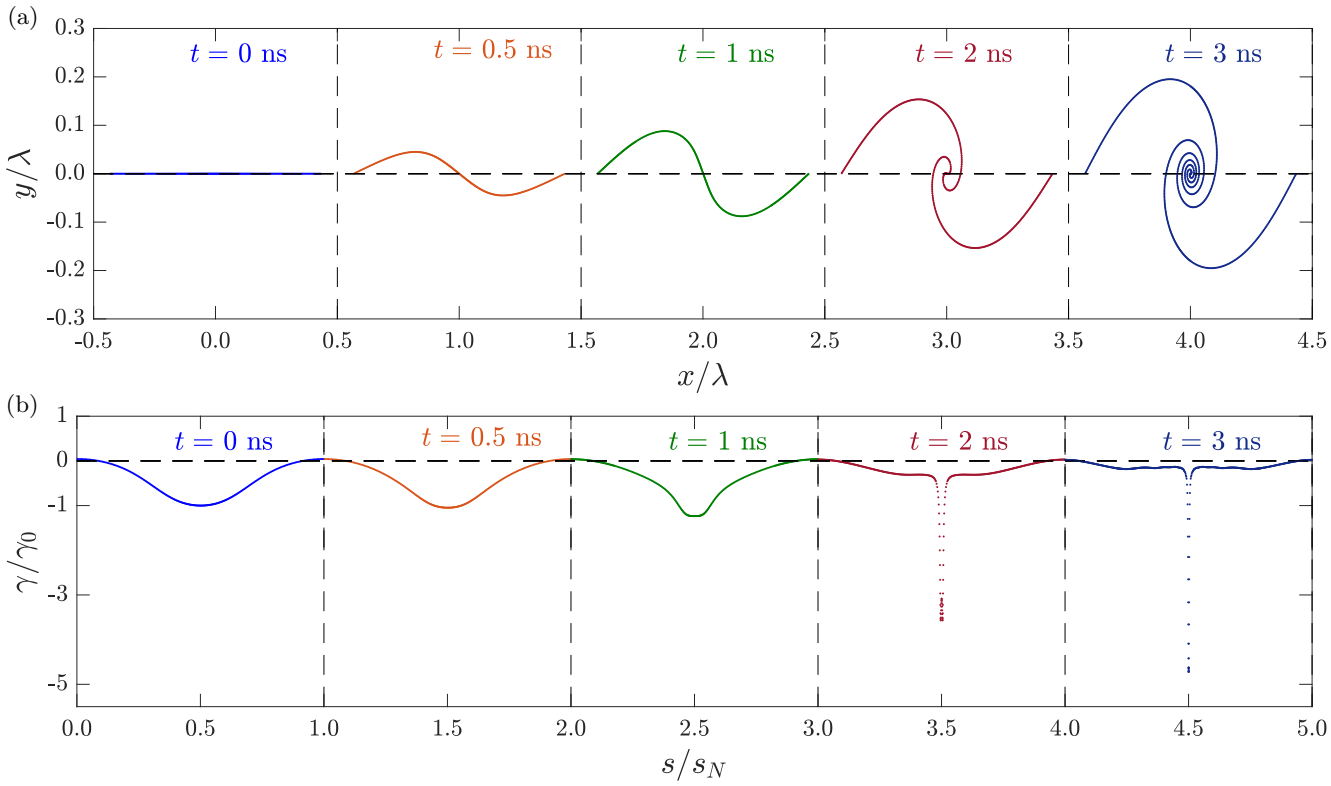

FIG. 12: Time evolution of (a) the interface and (b) associated sheet-strength distribution for the baseline case ($\theta = 30°$) when solving the kinematics coupled with the dynamics assuming $A = 0$.

pression) to the experiments and the xRAGE simulations. Both vortex-sheet solutions give similar results until $t \approx 5$ ns, at which point the rarefaction produced by laser turn-off reaches the interface. When not accounting for this deceleration, the vortex-sheet solution predicts a growth saturation, contrary to the experiments and the simulations. When accounting for the laser-induced deceleration and interface decompression, relatively good agreement with the late-time behavior predicted by the xRAGE simulations is achieved. The overprediction of the vortex-sheet solution accounting for laser-induced effects (red curve) may come from a slight overprediction of the total circulation at the time at which the shock leaves the interface. The total circulation may be affected by additional vorticity along the transmitted shock, thus slightly overpredicting the initial growth rate.

DATA AVAILABILITY STATEMENT

The data that support the findings of this study are available from the corresponding author upon reasonable request.

REFERENCES

[1]L. Rayleigh, Cambridge Univ. Press , 441 (1900).
[2]G. I. Taylor, Proc. R. Soc., Series A. **201**, 192 (1950).
[3]R. D. Richtmyer, Commun. Pur. Appl. Math **13**, 297 (1960).
[4]E. Meshkov, Fluid Dyn. **4**, 101 (1969).
[5]W. Thomson (Lord Kelvin), Philos. Mag **42**, 362 (1871), https://doi.org/10.1080/14786447108640585.
[6]H. Helmholtz, Philos. Mag **36**, 337 (1868), https://doi.org/10.1080/14786446808640073.
[7]N. Meezan, A. MacKinnon, D. Hicks, E. Dewald, R. Tommasini, S. Le Pape, T. Döppner, T. Ma, D. Farley, D. Kalantar, *et al.*, Phys. Plasmas **20**, 056311 (2013).
[8]D. Hicks, N. Meezan, E. Dewald, A. Mackinnon, R. Olson, D. Callahan, T. Döppner, L. Benedetti, D. Bradley, P. Celliers, *et al.*, Phys. Plasmas **19**, 122702 (2012).
[9]S. I. Abarzhi, A. K. Bhowmick, A. Naveh, A. Pandian, N. C. Swisher, R. F. Stellingwerf, and W. D. Arnett, Proceedings of the National Academy of Sciences , 201714502 (2018).
[10]J. Kane, D. Arnett, B. Remington, S. Glendinning, J. Castor, R. Wallace, A. Rubenchik, and B. Fryxell, ApJ **478**, L75 (1997).
[11]J. R. Johnson, S. Wing, and P. A. Delamere, Space Sci. Rev. **184**, 1 (2014).
[12]R. P. Drake, Plasma Phys. Control. Fusion **47**, B419 (2005).
[13]D. Ryutov and B. Remington, Plasma Phys. Control. Fusion **44**, B407 (2002).
[14]B. A. Remington, Plasma Phys. Control. Fusion **47**, A191 (2005).
[15]B. A. Remington, H.-S. Park, D. T. Casey, R. M. Cavallo, D. S. Clark, C. M. Huntington, C. C. Kuranz, A. R. Miles, S. R. Nagel, K. S. Raman, *et al.*, Proceedings of the National Academy of Sciences **116**, 18233 (2019).

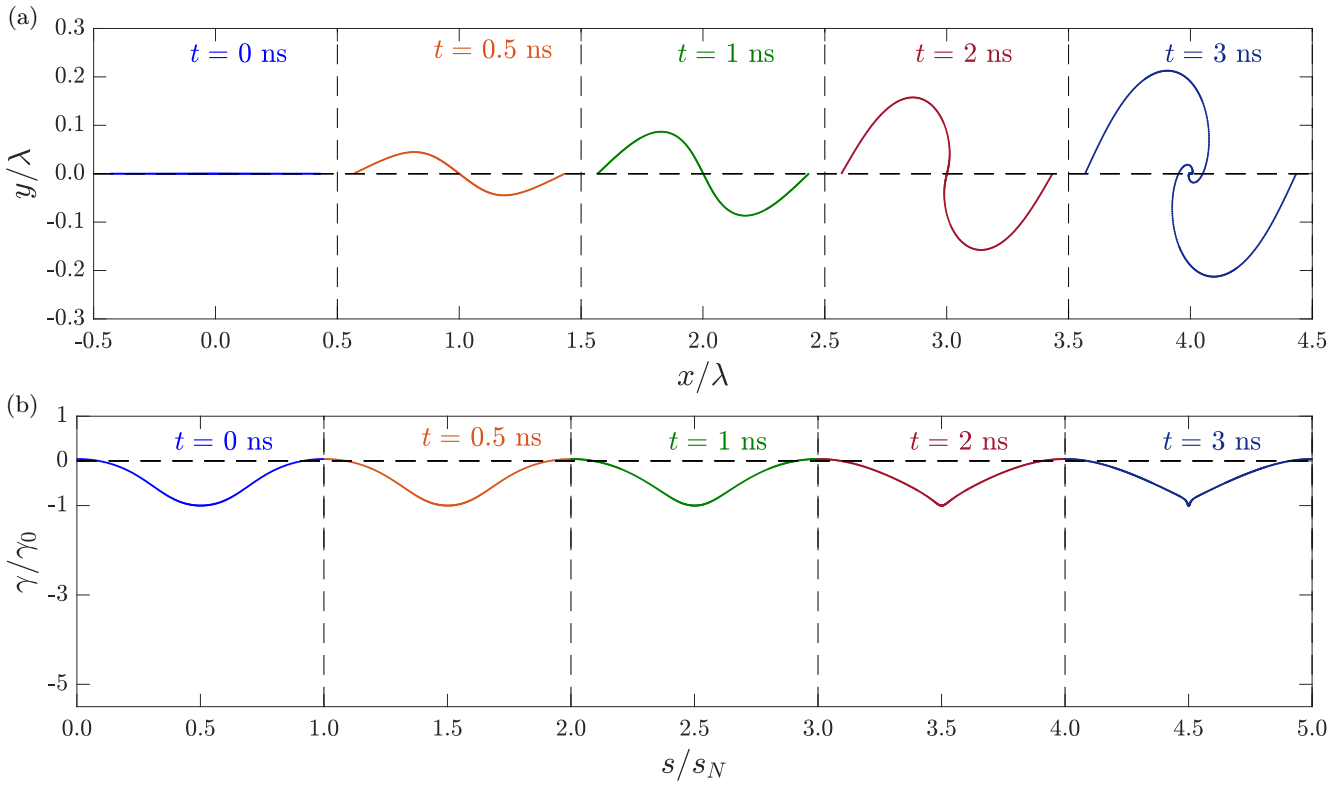

FIG. 13: Time evolution of (a) the interface and (b) associated sheet-strength distribution for the baseline case ($\theta = 30°$) when solving the kinematics only.

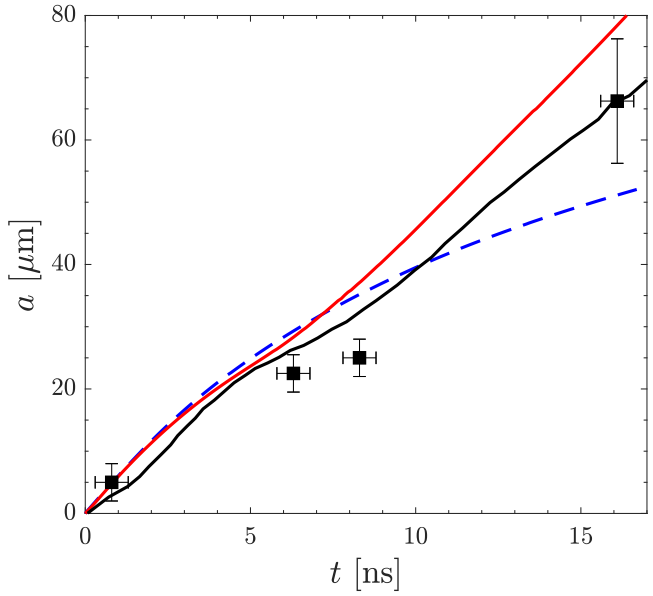

FIG. 14: Time evolution of the perturbation amplitude obtained from the vortex sheet, without laser-induced deceleration or decompression due to laser turn-off (- - -), with both deceleration and decompression (—), the experiments (■), and xRAGE simulations[69] (—).

[16] C. Kuranz, R. Drake, E. Harding, M. Grosskopf, H. Robey, B. Remington, M. Edwards, A. Miles, T. Perry, B. Blue, *et al.*, ApJ **696**, 749 (2009).
[17] J. W. Jacobs and V. Krivets, Phys. Fluids **17**, 034105 (2005).
[18] J. W. Jacobs and I. Catton, J. Fluid Mech **187**, 329 (1988).
[19] J. W. Jacobs and I. Catton, J. Fluid Mech **187**, 353 (1988).
[20] Y. Zhou, Phys. Rep **720-722**, 1 (2017).
[21] Y. Zhou, Phys. Rep **723-725**, 1 (2017).
[22] G. Malamud, C. Di Stefano, Y. Elbaz, C. Huntington, C. Kuranz, P. Keiter, and R. Drake, High Energ. Dens. Phys **9**, 122 (2013).
[23] C. Di Stefano, G. Malamud, C. Kuranz, S. Klein, C. Stoeckl, and R. Drake, Appl. Phys. Lett **106**, 114103 (2015).
[24] C. A. Di Stefano, G. Malamud, C. Kuranz, S. Klein, and R. Drake, High Energ. Dens. Phys **17**, 263 (2015).
[25] S. R. Nagel, K. S. Raman, C. M. Huntington, S. A. MacLaren, P. Wang, M. A. Barrios, T. Baumann, J. Bender, L. Benedetti, D. Doane, *et al.*, Phys. Plasmas **24**, 072704 (2017).
[26] G. Dimonte, C. E. Frerking, M. Schneider, and B. Remington, Phys. Plasmas **3**, 614 (1996).
[27] Y. Aglitskiy, N. Metzler, M. Karasik, V. Serlin, A. Velikovich, S. Obenschain, A. Mostovych, A. Schmitt, J. Weaver, J. Gardner, *et al.*, Phys. Plasmas **13**, 080703 (2006).
[28] Y. Aglitskiy, A. Velikovich, M. Karasik, N. Metzler, S. Zalesak, A. Schmitt, L. Phillips, J. Gardner, V. Serlin, J. Weaver, *et al.*, Philos. Trans. R. Soc. A. **368**, 1739 (2010).
[29] E. Harding, J. Hansen, O. Hurricane, R. Drake, H. Robey, C. Kuranz, B. Remington, M. Bono, M. Grosskopf, and R. Gillespie, Phys. Rev. Lett **103**, 045005 (2009).
[30] O. Hurricane, High Energ. Dens. Phys **4**, 97 (2008).
[31] K. Flippo, F. Doss, E. Merritt, B. DeVolder, C. Di Stefano, P. Bradley, D. Capelli, T. Cardenas, T. Desjardins, F. Fierro, *et al.*, Physics of Plasmas **25**, 056315 (2018).

[32]F. Doss, K. Flippo, E. Merritt, B. DeVolder, C. Di Stefano, C. Huntington, J. Kline, L. Kot, S. Nagel, A. Rasmus, *et al.*, Phys. Plasmas **27**, 032701 (2020).
[33]G. Malamud, A. Shimony, W. Wan, C. Di Stefano, Y. Elbaz, C. Kuranz, P. Keiter, R. Drake, and D. Shvarts, High Energ. Dens. Phys **9**, 672 (2013).
[34]W. Wan, G. Malamud, A. Shimony, C. Di Stefano, M. Trantham, S. Klein, D. Shvarts, C. Kuranz, and R. Drake, Phys. Rev. Lett **115**, 145001 (2015).
[35]W. Wan, G. Malamud, A. Shimony, C. Di Stefano, M. Trantham, S. Klein, D. Shvarts, R. Drake, and C. Kuranz, Phys. Plasmas **24**, 055705 (2017).
[36]A. M. Rasmus, C. A. Di Stefano, K. A. Flippo, F. W. Doss, J. L. Kline, J. D. Hager, E. C. Merritt, T. R. Desjardins, W. C. Wan, T. Cardenas, *et al.*, Phys. Plasmas **25**, 032119 (2018).
[37]A. M. Rasmus, C. A. Di Stefano, K. A. Flippo, F. W. Doss, C. F. Kawaguchi, J. Kline, *et al.*, Phys. Plasmas **26**, 062103 (2019).
[38]N. J. Zabusky, Annu. Rev. Fluid Mech. **31**, 495 (1999).
[39]M. Brouillette, Annu. Rev. Fluid Mech. **34**, 445 (2002).
[40]P. G. Saffman, *Vortex dynamics* (Cambridge University Press, 1992).
[41]C. Pozrikidis, *Introduction to theoretical and computational fluid dynamics* (Oxford university press, 2011).
[42]Y. Yang, Q. Zhang, and D. H. Sharp, Phys. Fluids **6**, 1856 (1994).
[43]J. G. Wouchuk and K. Nishihara, Phys. Plasmas **3**, 3761 (1996).
[44]J. G. Wouchuk and K. Nishihara, Phys. Plasmas **4**, 1028 (1997).
[45]Q. Zhang and S.-I. Sohn, Phys. Lett. A **212**, 149 (1996).
[46]Q. Zhang and S.-I. Sohn, Phys. Fluids **9**, 1106 (1997).
[47]U. Alon, J. Hecht, D. Ofer, and D. Shvarts, Phys. Rev. Lett **74**, 534 (1995).
[48]D. Oron, L. Arazi, D. Kartoon, A. Rikanati, U. Alon, and D. Shvarts, Phys. Plasmas **8**, 2883 (2001).
[49]L. Rosenhead, Proc. R. Soc. Lond. A **134**, 170 (1931).
[50]G. R. Baker, D. I. Meiron, and S. A. Orszag, J. Fluid Mech. **123**, 477 (1982).
[51]J. J. Higdon and C. Pozrikidis, J. Fluid Mech. **150**, 203 (1985).
[52]C. Pozrikidis, J. Fluid Mech. **425**, 335 (2000).
[53]S.-I. Sohn, D. Yoon, and W. Hwang, Phys. Rev. E **82**, 046711 (2010).
[54]R. Krasny, J. Fluid Mech. **167**, 65 (1986).
[55]R. Krasny, J. Comput. Phys. **65**, 292 (1986).
[56]R. Krasny, J. Fluid Mech. **184**, 123 (1987).
[57]G. Tryggvason, J.Comput. Phys. **80**, 1 (1989).
[58]G. Tryggvason, J. Comput. Phys. **75**, 253 (1988).
[59]S.-I. Sohn, J. Phys. Soc. Japan **80**, 084401 (2011).
[60]S.-I. Sohn, Phys. Rev. E **69**, 036703 (2004).
[61]J. A. Zufiria, Phys. Fluids **31**, 3199 (1988).
[62]C. Matsuoka, K. Nishihara, and Y. Fukuda, Phys. Rev. E **67**, 036301 (2003).
[63]C. Matsuoka and K. Nishihara, Phys. Rev. E **73**, 026304 (2006).
[64]R. Samtaney and N. J. Zabusky, J. Fluid Mech. **269**, 45 (1994).
[65]G. H. Cottet and P. D. Koumoutsakos, *Vortex methods: theory and practice* (Cambridge University Press, 2000).
[66]H. Feng, L. Kaganovskiy, and R. Krasny, Fluid Dyn. Res. **41**, 051405 (2009).
[67]S. G. Glendinning, J. Bolstad, D. Braun, M. Edwards, W. Hsing, B. Lasinski, H. Louis, A. Miles, J. Moreno, T. Peyser, *et al.*, Phys. Plasmas **10**, 1931 (2003).
[68]M. Gittings, R. Weaver, M. Clover, T. Betlach, N. Byrne, R. Coker, E. Dendy, R. Hueckstaedt, K. New, W. R. Oakes, *et al.*, Comput. Sci. Discov **1**, 015005 (2008).
[69]C. A. Di Stefano, F. W. Doss, A. M. Rasmus, K. A. Flippo, and B. M. Haines, Phys. Plasmas **26**, 052708 (2019).
[70]G. Peng, N. J. Zabusky, and S. Zhang, Phys. Fluids **15**, 3730 (2003).
[71]B. M. Haines, E. L. Vold, K. Molvig, C. Aldrich, and R. Rauenzahn, Phys. Plasmas **21**, 092306 (2014).
[72]K. O. Mikaelian, Phys. Fluids **6**, 1943 (1994).
[73]J. Marozas, M. Hohenberger, M. Rosenberg, D. Turnbull, T. Collins, P. Radha, P. McKenty, J. Zuegel, F. Marshall, S. Regan, *et al.*, Phys. Plasmas **25**, 056314 (2018).
[74]B. Haines, G. Grim, J. Fincke, R. Shah, C. Forrest, K. Silverstein, F. Marshall, M. Boswell, M. Fowler, R. Gore, *et al.*, Phys. Plasmas **23**, 072709 (2016).